25. T. Zhang *et al.*, *Hum. Mol. Genet.* **22**, 1262–1269 (2013).
26. Y. Huang *et al.*, *Gastroenterology* **132**, 733–744 (2007).
27. B. P. Doehle, A. Schäfer, B. R. Cullen, *Virology* **339**, 281–288 (2005).
28. G. Berger *et al.*, *PLOS Pathog.* **7**, e1002221 (2011).
29. H. Muckenfuss *et al.*, *J. Biol. Chem.* **281**, 22161–22172 (2006).
30. C. Münk, A. Willemsen, I. G. Bravo, *BMC Evol. Biol.* **12**, 71 (2012).
31. M. A. Carpenter *et al.*, *J. Biol. Chem.* **287**, 34801–34808 (2012).
32. P. Turelli, B. Mangeat, S. Jost, S. Vianin, D. Trono, *Science* **303**, 1829 (2004).
33. C. T. Bock *et al.*, *J. Mol. Biol.* **307**, 183–196 (2001).
34. M. M. Aynaud *et al.*, *J. Biol. Chem.* **287**, 39182–39192 (2012).
35. Y. Guo *et al.*, *BMC Genomics* **13**, 563 (2012).
36. H. C. Smith, R. P. Bennett, A. Kizilyer, W. M. McDougall, K. M. Prohaska, *Semin. Cell Dev. Biol.* **23**, 258–268 (2012).
37. T. H. Lee, S. J. Elledge, J. S. Butel, *J. Virol.* **69**, 1107–1114 (1995).
38. K. Kitamura *et al.*, *PLOS Pathog.* **9**, e1003361 (2013).
39. S. Landry, I. Narvaiza, D. C. Linfesty, M. D. Weitzman, *EMBO Rep.* **12**, 444–450 (2011).
40. M. B. Burns *et al.*, *Nature* **494**, 366–370 (2013).
41. K. Krebs *et al.*, *Gastroenterology* **145**, 456–465 (2013).

Acknowledgments: We thank R. Bester, T. Asen, K. Ackermann, K. Kappes, M. Feuerherd, R. Baier, R. Hillermann, U. Finkel, A. Krikoni, and F. Zhang for technical support; L. Terracciano for analysis of acute hepatitis patients; F. Chisari for HBV transgenic mice (HBV 1.3.32); T. Buch and O. Prazeres da Costa for help with array analysis and data discussions; L. Allweiss and A. Groth for help in generating and treating humanized uPA-SCID mice; and Siemens Healthcare Diagnostics for reagents. Supported by grants from Fédération Belge Contre le Cancer (E.D.), a European Research Council starting grant (LiverCancerMechanism) (M.H.), the German Research Foundation (SFB 841 to M.D., SFB TR 36 to M.H., and SFB TR 22), the Peter-Hans Hofschneider Foundation and the Helmholtz Alliances HAIT (U.P.), and PCCC (M.H.). We acknowledge the support of the nonprofit foundation HTCR, which holds human tissue on trust, making it broadly available for research on an ethical and legal basis. Patent application EP12006XXX has been filed at the European patent office: "Lymphotoxin signaling activation and its downstream mediators eliminate HBV ccc DNA." Microarray data have been submitted to the GEO database (www.ncbi.nlm.nih.gov/geo/) with accession number GSE46667. Human liver chimeric uPA-SCID mice were handled in accordance with protocols approved by the ethical committee of the city and state of Hamburg (permission number G12/015). Experiments with HBV-transgenic mice were performed in accordance with German legislation governing animal studies and the Principles of Laboratory Animal Care guidelines, NIH (55.1-1-54-2531.3-27-08). The study protocol for the animal experiment in fig. S12B was approved at the Southwest Foundation for Biomedical Research, San Antonio, TX (IACUC 869 PT, approved in 2004).

Supplementary Materials

www.sciencemag.org/content/343/6176/1221/suppl/DC1
Materials and Methods
Figs. S1 to S21
Table S1
References (*42*–*62*)

18 July 2013; accepted 5 February 2014
Published online 20 February 2014;
10.1126/science.1243462

REPORTS

Free-Standing Single-Atom-Thick Iron Membranes Suspended in Graphene Pores

Jiong Zhao,[1,3] Qingming Deng,[2] Alicja Bachmatiuk,[1,3,4] Gorantla Sandeep,[1] Alexey Popov,[2] Jürgen Eckert,[1,5] Mark H. Rümmeli[3,6]*

The excess of surface dangling bonds makes the formation of free-standing two-dimensional (2D) metals unstable and hence difficult to achieve. To date, only a few reports have demonstrated 2D metal formation over substrates. Here, we show a free-standing crystalline single-atom-thick layer of iron (Fe) using in situ low-voltage aberration-corrected transmission electron microscopy and supporting image simulations. First-principles calculations confirm enhanced magnetic properties for single-atom-thick 2D Fe membranes. This work could pave the way for new 2D structures to be formed in graphene membranes.

The success and promise of atomically thin carbon–namely, graphene (*1*)–has triggered enormous enthusiasm for the study of other two-dimensional (2D) materials such as hBN, MoS_2, and $MoSe_2$ (*2*, *3*). These 2D films are able to be reduced to atomically thin layers while still maintaining mechanical integrity, because they are layered structures where the bonding within a layer is covalent whereas the interlayer bonding occurs through weak van der Waals interactions, thus allowing individual layers to be easily separated. With bulk metals, at first glance, the nature of metallic bonding and their 3D structure prohibit them from existing as a monoatomic layer. The only reports for atomically thin metallic layers, thus far, are heteroepitaxial structures in which the metal atoms bond with the underlying substrates (*4*, *5*). On the other hand, because of nondirectional metallic bonding and the excellent plasticity of metals, at the nanoscale, one can build few-atom or even single-atom bridges (*6*, *7*). Many single atomic metallic layers (e.g., Fe, Co, and Mn) are attractive due to their inherent magnetic properties. For the case of 2D Fe monolayers, the magnetic moment is expected to be 3.1 μB, which is markedly higher than its bulk counterpart (2.2 μB), and, in addition, 2D Fe should have a large perpendicular magnetic anisotropy (*8*). Hence, 2D magnets could be promising for magnetic recording media. Most of what is known about 2D magnets is based on theoretical investigations. These studies point to their magnetic properties being highly sensitive to their structure (*9*). Face-centered cubic (FCC) Fe and body-centered cubic (BCC) Fe ultrathin films have been grown on Cu, W, SiC, MgO, and other surfaces (*9*–*13*). However, these structures interact with the underlying substrate. Free-standing 2D metal films do not suffer from substrate-based influences, thus preserving coordination and electron confinement.

Experimental and theoretical works have focused on the interactions between graphene and single metal atoms (including Fe atoms) (*14*–*16*) or clusters (*17*). We show that porous graphene under electron-beam irradiation can be extended to enable Fe atoms and clusters to entirely seal small perforations in graphene and form a single atomic crystalline Fe layer.

In our in situ investigation, a low-voltage spherical aberration-corrected transmission electron microscopy (LVACTEM) operating with an acceleration voltage of 80 kV was employed (*18*). The graphene samples were grown by chemical vapor deposition (CVD) over Ni/Mo substrates (*19*). The as-produced monolayer graphene was then transferred on to standard lacey carbon (TEM) grids using an $FeCl_3$ etching solution to detach the graphene (*20*). The transferred samples typically consist of large areas of monolayer graphene in which some regions contain remnant material from the transfer process, including remnant Fe species from decomposed $FeCl_3$ (*20*). Under close inspection, pure Fe can be found as small nanocrystals forming on the surface of the graphene, as single atoms or small clusters at the edge of pores in clean graphene, or as 2D crys-

[1]Leibniz-Institut für Festkörper- und Werkstoffforschung Dresden (IFW) Dresden, Institute of Complex Materials, P.O. Box 270116, D-01171 Dresden, Germany. [2]IFW Dresden, Institute of Solid State Research, P.O. Box 270116, D-01171 Dresden, Germany. [3]IBS Center for Integrated Nanostructure Physics, Institute for Basic Science (IBS), Daejon 305-701, Republic of Korea. [4]Centre of Polymer and Carbon Materials, Polish Academy of Sciences, M. Curie-Sklodowskiej 34, Zabrze 41-819, Poland. [5]Technische Universität Dresden, Institute of Materials Science, 01062 Dresden, Germany. [6]Department of Energy Science, Department of Physics, Sungkyunkwan University, Suwon 440-746, Republic of Korea.

*Corresponding author. E-mail: mark@rummeli.com

talline membranes suspended across perforations in the graphene. Typical examples are provided in Fig. 1. In the case of nanocrystalline structures forming on the surface of the graphene (Fig. 1, B and C), the measured lattice constants obtained from the Fourier domain from numerous micrographs indicates that they are either BCC or hexagonal close-packed (HCP) Fe structures. These structures match image simulations of BCC and HCP Fe nanocrystals as, for example, shown in the insets of Fig. 1, B and C, in which both the stick-and-ball models and image simulations are provided. In general, the Fe nanocrystals contain 200 to 1000 Fe atoms. Local electron energy-loss spectroscopy (EELS) spectra highlight the presence of pure Fe clusters (figs. S1 and S2). Detailed investigations at the local scale exclude other possible compounds—e.g., carbides and oxides—and confirm the presence of pure Fe nanostructures. Representative studies are provided in figs. S3 to S6.

In the case of individual Fe atoms or few-atom clusters, they tend to get trapped in small vacancies and pores in the graphene and are easily visible due to their high contrast relative to the graphene lattice. Typical examples are provided in Fig. 1D (Fe cluster in a pore) and Fig. 1E (individual atoms trapped at pore edges). Typically, these atoms are mobile around the edges when irradiated with electrons. These observations have been reported by others (*14*), so we do not elaborate further. What we do focus on here is the ability of larger numbers of Fe atoms to get trapped within a pore and form an ordered 2D crystalline lattice. Examples of such 2D Fe crystalline structures can easily be seen in Fig. 1, F and G, where the high-contrast Fe atoms fill a pore with the atoms arranging themselves, for the most part, in an ordered manner. The lattice constant for the observed nanocrystals is 2.65 ± 0.05 Å, which is appreciably larger than that for the (200) Miller-index plane distance for the FCC phase or the (110) plane distance for BCC Fe.

Figure 2A shows a higher-magnification TEM micrograph of one of these Fe membranes suspended in a graphene pore. Figure 2B shows the corresponding micrograph after Fourier transform filtering (to reduce noise), and Fig. 2C shows an image simulation of a 2D Fe membrane suspended in graphene. Initial visual inspection shows strong similarities. Figure 2D shows the

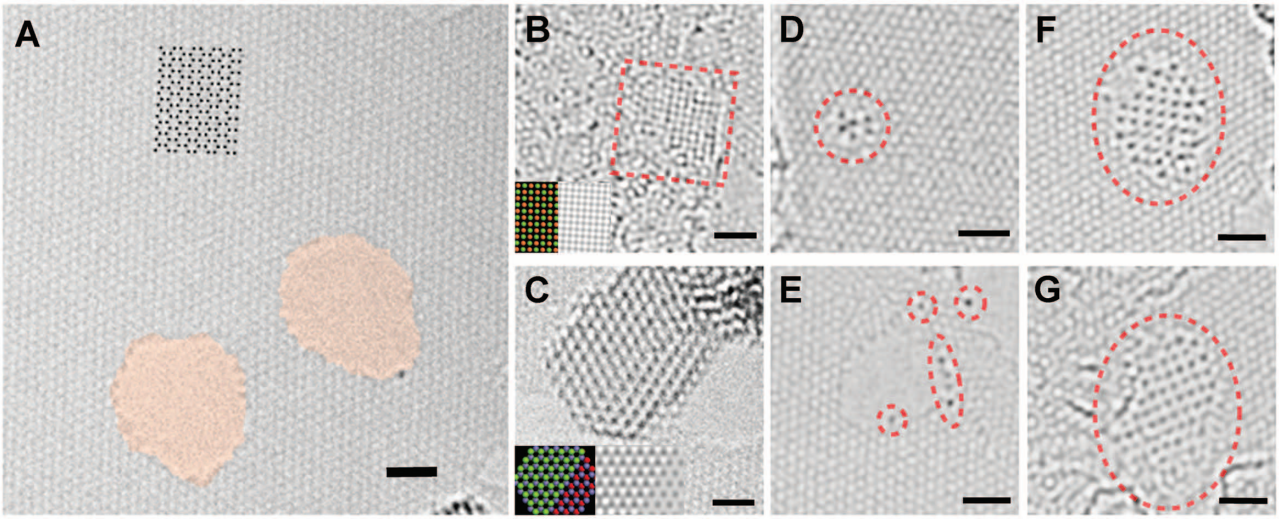

Fig. 1. LVACTEM images of graphene perforations and various Fe clusters. (**A**) Graphene perforations (highlighted). (**B**) BCC Fe nanocrystal, with atomic structure and image simulation as an inset. (**C**) HCP Fe nanocrystal, which has a step on it. The atomic structure and an image simulation are provided in the inset. (**D**) A several-atom cluster embedded in graphene. (**E**) Many individual Fe atoms residing on the edges of graphene. (**F** and **G**) Two typical monoatomic Fe layers suspended in a perforation in graphene. Scale bars, 1 nm.

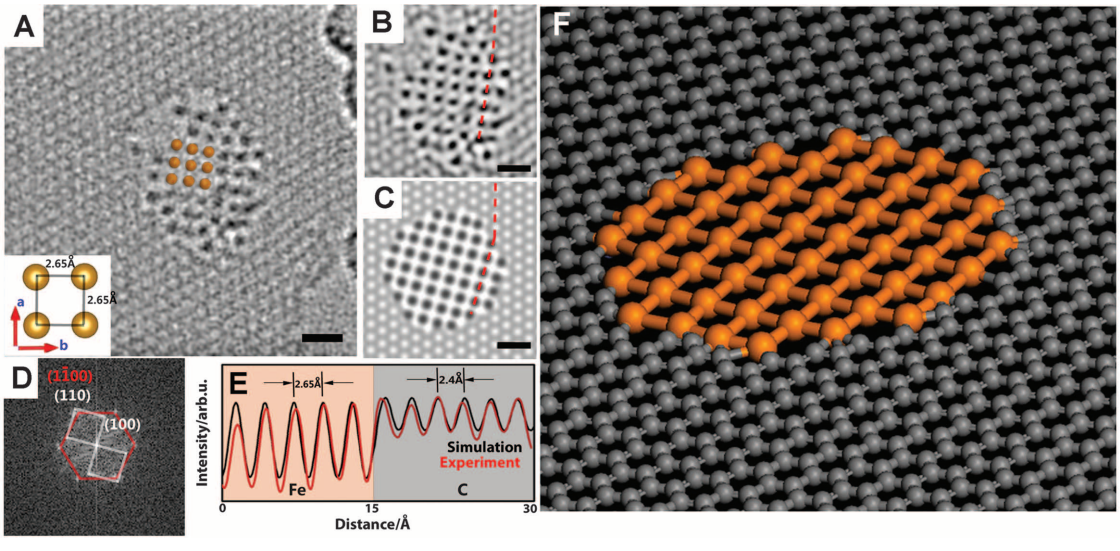

Fig. 2. Characterization of monoatomic Fe layer. (**A**) LVACTEM micrograph of a monoatomic Fe layer with the square unit cell. The inset highlights the interatomic spacing of the square unit cell. (**B**) Smoothed image of (A). (**C**) Image simulation of a monoatomic Fe layer. (**D**) Fast Fourier transform of the structure in (A) that shows the lattice relationship between the graphene (red) and the monoatomic Fe layer (white). (**E**) Normalized intensity profiles from the image simulation (black line) and experimental image (red line), corresponding to marked profiles in red dashed lines in (B) and (C). The intensity profiles match, confirming that the Fe membrane is a single atom thick. (**F**) Atomic structure of a suspended mono/atomic Fe layer in a graphene pore. All scale bars, 0.6 nm.

Fourier transform of Fig. 2A. The inner reflexes correspond to the (100) plane of Fe. The outer reflexes arise from the (1-100) plane of graphene. In addition, the (110) plane for Fe almost overlaps the (1-100) graphene planes. This indicates preferential alignment of the Fe(110) plane with the graphene (1-100) plane. This preferential alignment was observed for all the examined structures. We also compared the relative intensity variation between the graphene basal plane and the Fe structure filling the pore for both the experimentally obtained micrographs and the image simulations. An example is provided in Fig. 2E. The two profiles match each other extremely well. The image simulation is formed from a single atomic layer of Fe atoms (Fig. 2F) and so confirms that the suspended Fe structure we measure experimentally is a single-atom-thick Fe layer with a square lattice (see fig. S7 for more detail on thickness determination). EELS studies show only Fe peaks and no carbon or oxygen signatures, confirming that the monolayer membranes are made only of Fe.

To better comprehend these monolayer Fe structures, we conducted density functional theory (DFT) calculations based on the generalized gradient approximation with the Perdew-Burke-Ernzerhof function (*21*). The calculations show that the in-plane square lattice of monolayer Fe is energetically favored over the other possible 2D configurations, including tetragonal, hexagonal, and so forth. The calculations suggest the most stable lattice constant for monolayer Fe is ~2.35 Å, which is smaller than our experimental value of 2.65 ± 0.05 Å; however, the calculated energy difference between 2.35 Å and 2.65 Å is not large (0.2 eV per atom) (table S1). In addition, some physical aspects not considered in the calculations could lead to a larger lattice constant. For example, the effect of spin-orbit coupling and perpendicular magnetic anisotropy in atomically thin films will lead to energy variations. More important, strain due to lattice alignment and mismatch between graphene and 2D monolayer Fe cannot be ignored, particularly because our calculations show that the in-plane Young's modulus of monolayer iron is ~160 GPa, which is an order of magnitude smaller than that of graphene (1 TPa). Figures S8 to S11 and their accompanying discussion in the supplementary materials illustrate the effect of strain on the lattice spacing. Moreover, the phonons in monolayer Fe will differ from bulk 3D Fe (*22*) because the fraction of anharmonic vibrations increases with the reduction of thin-film thickness, which leads to a larger thermal expansion. To investigate this, an additional self-consistent lattice dynamics calculation or ab initio molecular dynamics calculation would be required (*23*).

One can get a sense of local strain effects by first looking at the interface between iron atoms attached to different graphene edges. Two possible binding configurations are possible between Fe atoms and graphene, namely, binding to the basal plane or at an open end or edge. In practice, binding at the basal plane is relatively common, whereas metallic atom binding at the open edges is rare even though such binding has been theoretically proposed (*24*). In our observations, the Fe atoms always bind at open graphene edges—for example, at the edges of a pore as shown in Fig. 3, A to C. We also study such Fe atom attachments using first-principle DFT calculations. Because the most stable edge terminations for graphene are the armchair and zigzag configurations (*25*), we investigated six possible configurations for single Fe atoms at armchair or zigzag edges, including an arrangement in which Fe atoms replace the first two rows of carbon atoms at an open edge (Fig. 3, D to I). The bonding energies of the Fe atoms for these config-

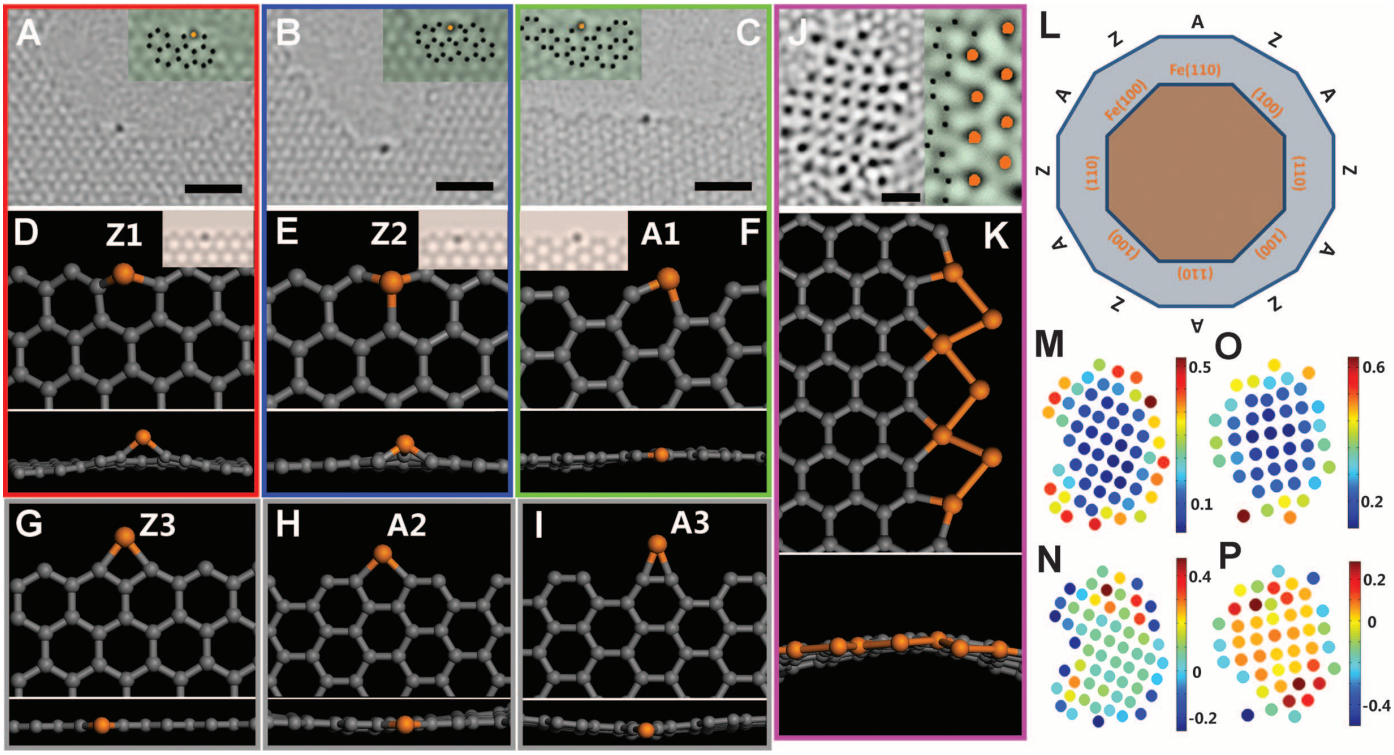

Fig. 3. The interface between a monoatomic Fe layer and graphene and local strain mapping. (**A**) LVACTEM image of the Z1 configuration as illustrated in (D). The insets show the highlighted edge structure, with carbon (black) atoms and Fe (orange) atoms highlighted. (**B** and **C**) LVACTEM images of the Z2 and A1 configurations [(E) and (F), respectively]. The insets show the highlighted edge structure with carbon (black) atoms and Fe (orange) atoms highlighted. Scale bars in (A) to (C), 1 nm. (**D** to **I**) First-principle calculation results showing top and cross-section views of different single-Fe atoms binding to different graphene-edge configurations. The insets for (D) to (F) show the corresponding image simulations from the stick-and-ball structure provided in the main panels. (**J** and **K**) The Fe(110) with armchair edge visible in a LVACTEM image and first-principle-calculated configuration, respectively. Scale bar in (J), 0.5 nm. (**L**) Schematic diagram showing the relationship between the (100) and (110) Fe edges and the zigzag (Z) and armchair (A) edges from graphene. (**M** to **P**) Calculated local von Mises-strain-invariant plots of two single-atom Fe layers. The atom positions are taken from the micrographs provided in Fig. 1, F and G; (M) and (O) provide the hydrostatic strain plots, and (N) and (P) show the shear strain plots. The color of each atom refers to the values in the vertical scale bar.

urations are provided in table S2. Despite the bonding energies not being at a minimum in the substitution configuration in which an Fe atom replaces a single carbon atom in a hexagonal ring (configurations Z1, Z2, and A1 in Fig. 3, D to F, respectively), as compared to configurations Z3, A2, and A3 (Fig. 3, G to I, respectively), they are favored because upon removal of an Fe atom, an incomplete hexagon structure is left, which is energetically unfavorable (as compared to zigzag or armchair terminations). Thus, the reaction barrier for the removal of substitution Fe atoms is high. Indeed, this is what we observe experimentally, where for the most part, Fe atoms are imaged as substituting a C atom in a benzene ring at the edge of graphene, as shown in Fig. 3, A to C. For comparison, image simulations based on the structures used for the first-principles calculations are provided as insets in Fig. 3, D to F.

Although substitution configurations are more stable, the formation of an Fe monoatomic layer occurs with a continuous placement of Fe atoms along the edges that are not always set in a substitution configuration. For example, linking configurations such as Z3 (Fig. 3G) and A2 (Fig. 3H) are also found, as can be seen in Fig. 3J. The linking formation shown in Fig. 3I is rarely observed; this is due to its reduced bonding energy. Linking formations are observed in monolayer Fe-graphene junctions, as illustrated in Fig. 3J; the corresponding calculated structure is also given (Fig. 3K).

Another aspect to consider at the Fe membrane-graphene interface is the preferential alignment of Fe atoms. For example, considering the graphene zigzag and armchair edges and the lattice constant for monolayer Fe, the best lattice match is twice the Fe(110) plane distance (1.9 Å) with an armchair edge (2.1 Å). This configuration provides the lowest mismatch strain and interfacial energy and is an alignment configuration that we observe in our experiments, as can be seen in the diffraction information shown in Fig. 2D. However, if an Fe(110) plane to armchair configuration exists, then the only other match is for the Fe(110) plane to align with a zigzag edge (Fig. 3L). In effect, in a membrane interface, mismatches lead to distortions at the interface (within 15°). The interfacial distortions can be seen more clearly on local strain maps, as illustrated in Fig. 3, M to P. The atomistic positions are obtained by the Gaussian fitting of atom locations taken from experimental micrographs. The local 2D atomistic strains are then calculated (*26*). The shear strain components and hydrostatic strain components are provided in Fig. 3, M and O, and Fig. 3, N and P, respectively, for two actual images (Fig. 1, G and F, respectively). Examination of the strain maps show lower shear at the center of an Fe membrane than at the edges. This is concomitant with the hydrostatic strain, which appears homogeneous at the center of the membrane. (See the supplementary materials for further discussion.)

We now turn to the formation and stability of single-atom-thick Fe membranes while under electron irradiation. Typically, Fe atoms on the surface of the graphene are mobile while exposed to electron irradiation. If they encounter a small hole (a few nm wide), the atoms collect and rearrange themselves within it to form a monolayer crystalline Fe membrane. The formation process usually occurs in a matter of seconds. Figure 4A shows a hole in the graphene with a number of Fe atoms perched by an edge. After 3 s of electron irradiation (1 pA/nm^2), the Fe atoms have moved into the hole and arranged themselves neatly into a crystalline 2D Fe membrane (Fig. 4B). (A more detailed set of images and the formation of a suspended Fe monolayer by etching the graphene beneath can be found in figs. S12 to S14.) Once a suspended Fe membrane has formed in a graphene pore, it is relatively stable in that it can sustain electron irradiation for several minutes, after which it starts to collapse (Fig. 4, C to J). Closer examination shows that the Fe monolayer edge disconnects first from a zigzag edge, whereas Fe (110) membrane-armchair interfaces tend to remain stable for far longer before forming an amorphous particle (see circled regions in Fig. 4, E and F). This is in agreement with our analysis above, in which armchair interfaces are shown to be the most stable configurations.

We also studied the diameter-stability dependence. By investigating the energy difference, ΔE, between a suspended Fe monolayer and a nanoparticle using the equivalent number of Fe atoms, one can estimate the largest stable Fe membrane that can form. ΔE is given by

$$\Delta E = E_{Fe\text{-}C} + E_{MLFe} - E_{Fe} \qquad (1)$$

where $E_{Fe\text{-}C}$ is the binding energy between the Fe membrane and graphene interface, E_{MLFe} is the total energy of the Fe monolayer, and E_{Fe} is the total energy of the Fe nanoparticle, including the surface energy. Neglecting the effects of lattice instabilities and using energy values determined in our previous DFT calculations, we find the largest stable membrane to be ~12 atoms wide (fig. S15) or 3 by 3 nm^2. This is in excellent agreement with our experimental observation, in which the largest observed diameters are ~10 atoms.

Finally, we examined the band structure of a freestanding monolayer Fe membrane through spin-polarized DFT calculations using the experimentally derived lattice constant (2.65 Å) and compare it to the (calculated) band structure of bulk BCC Fe. Some obvious differences between the two can be seen, as shown in fig. S16. By comparing the partial density of states, one can see that for the spin-up (majority) orbitals, the d_z^2 orbital for 2D Fe is appreciably smaller than for bulk BCC Fe. This is primarily due to the 2D nature of the Fe membrane, because the d_z^2

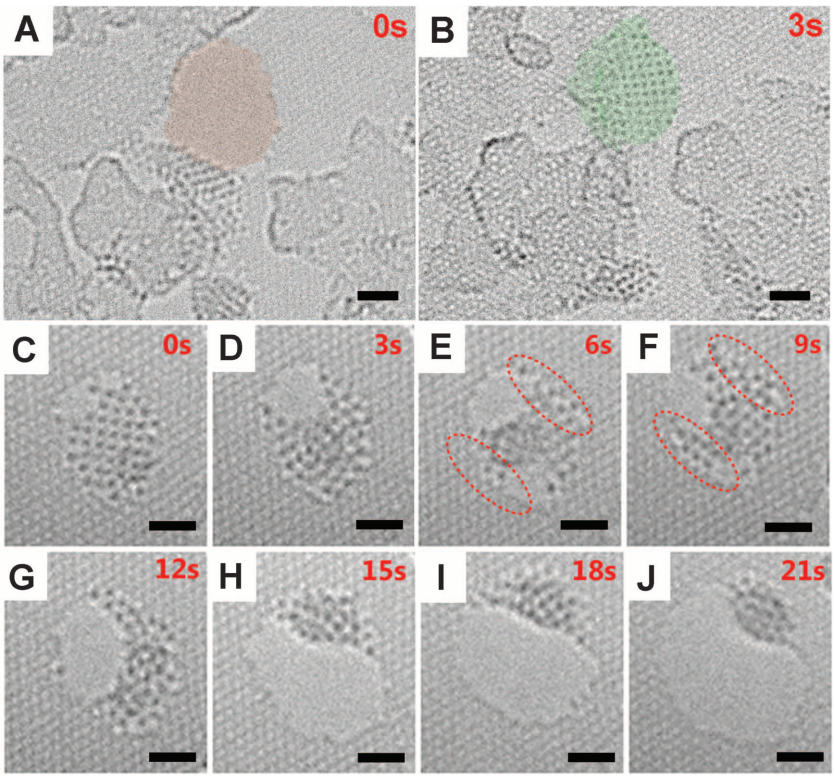

Fig. 4. The formation and collapse of a suspended single-atom Fe layer under electron irradiation. (**A**) An Fe cluster at the edge of a graphene pore (highlighted). (**B**) After 3 s, the Fe atoms move in to the perforation and form a single-atom Fe membrane sealing the entire graphene pore. (**C** to **J**) Continued electron irradiation leads to the collapse of the 2D Fe membrane. The Fe(110)–armchair graphene interfaces are the most stable and are highlighted in (E) and (F). All scale bars, 1 nm.

orbital is out of plane whereas the d_{xy} orbital is in plane. The first-principles calculations show a considerably enhanced magnetic moment for single-atom-thick Fe membranes (3.08 μB) as compared with bulk BCC Fe (2.1 μB), in good agreement with previously calculated values (*8*). The total magnetic moment is slightly decreased by the Fe-C boundary effect but is still much larger the bulk value (fig. S17).

In summary, the existence of free-standing monoatomic suspended Fe membranes is demonstrated. These 2D Fe nanomembranes are directly imaged and are shown to have a square lattice with a 2.65 Å lattice constant at room temperature. These studies provide valuable data for further more accurate and in-depth theoretical investigations. The potential of perforated graphene as a support for 2D membranes is shown, and one can anticipate new 2D structures from a variety of elements to emerge.

References and Notes

1. K. S. Novoselov *et al*., *Science* **306**, 666–669 (2004).
2. C. H. Jin, F. Lin, K. Suenaga, S. Iijima, *Phys. Rev. Lett.* **102**, 195505 (2009).
3. H. Komsa, A. V. Krasheninnikov, *J. Phys. Chem. Lett.* **3**, 3652–3656 (2012).
4. D. Qian, X. F. Jin, J. Barthel, M. Klaua, J. Kirschner, *Phys. Rev. Lett.* **87**, 227204 (2001).
5. G. Wedler, C. M. Schneider, A. Trampert, R. Koch, *Phys. Rev. Lett.* **93**, 236101 (2004).
6. H. Ohnishi, Y. Kondo, K. Takayanagi, *Nature* **395**, 780–783 (1998).
7. M. J. Lagos, F. Sato, D. S. Galvão, D. Ugarte, *Phys. Rev. Lett.* **106**, 055501 (2011).
8. J. Izquierdo *et al*., *Phys. Rev. B* **61**, 13639–13646 (2000).
9. R. Lorenz, J. Hafner, *Phys. Rev. B* **54**, 15937–15949 (1996).
10. W. Lu, K. Zhang, X. Xie, *Phys. Rev. B* **48**, 18159–18163 (1993).
11. J. G. Gay, R. Richter, *Phys. Rev. Lett.* **56**, 2728–2731 (1986).
12. M. Wuttig, J. Thomassen, *Surf. Sci.* **282**, 237–245 (1993).
13. A. Lehnert *et al*., *Phys. Rev. B* **82**, 094409 (2010).
14. A. W. Robertson *et al*., *Nano Lett.* **13**, 1468–1475 (2013).
15. O. Cretu *et al*., *Phys. Rev. Lett.* **105**, 196102 (2010).
16. A. V. Krasheninnikov, P. O. Lehtinen, A. S. Foster, P. Pyykkö, R. M. Nieminen, *Phys. Rev. Lett.* **102**, 126807 (2009).
17. H. Wang *et al*., *Sci. Rep.* **2**, 995 (2012).
18. F. Börrnert *et al*., *J. Microsc.* **249**, 87–92 (2013).
19. B. Dai *et al*., *Nat. Commun.* **2**, 522 (2011).
20. Y. C. Lin *et al*., *ACS Nano* **5**, 2362–2368 (2011).
21. J. P. Perdew, K. Burke, M. Ernzerhof, *Phys. Rev. Lett.* **77**, 3865–3868 (1996).
22. S. Stankov *et al*., *Phys. Rev. Lett.* **99**, 185501 (2007).
23. G. Grimvall, B. Magyari-Köpe, V. Ozolins, K. A. Persson, *Rev. Mod. Phys.* **84**, 945–986 (2012).
24. Y. Matsuda, W. Deng, W. A. Goddard III, *J. Phys. Chem. C* **114**, 17845–17850 (2010).
25. Ç. Ö. Girit *et al*., *Science* **323**, 1705–1708 (2009).
26. J. Li, I. S. Yip, *Handbook of Materials Modeling* (Kluwer Academic Publishers, Dordrecht, Netherlands, 2005).

Acknowledgments: J.Z. thanks the Deutscher Akademischer Austausch Dienst DAAD Foundation, and S.G. thanks the Deutsche Forschungsgemeinschaft (RU 1540/8-1). thanks the DFG (project PO 1602/1-1 to A.P.). This work was supported by the Institute of Basic Science (IBS) Korea. We also thank Y.-h. Luo (East China University of Science and Technology) for providing us with the Dmol3 code. We thank S. Melkhanova and J. Pang for the fabrication of the CVD-grown graphene. We thank the IFW Dresden for granting us use of their microscopy facilities.

Supplementary Materials

www.sciencemag.org/content/343/6176/1228/suppl/DC1
Materials and Methods
Supplementary Text
Figs. S1 to S17
Tables S1 and S2
References (*27*–*33*)

28 August 2013; accepted 19 February 2014
10.1126/science.1245273

Main-Group Compounds Selectively Oxidize Mixtures of Methane, Ethane, and Propane to Alcohol Esters

Brian G. Hashiguchi,[1]* Michael M. Konnick,[1] Steven M. Bischof,[1] Samantha J. Gustafson,[2] Deepa Devarajan,[2] Niles Gunsalus,[1] Daniel H. Ess,[2]* Roy A. Periana[1]*

Much of the recent research on homogeneous alkane oxidation has focused on the use of transition metal catalysts. Here, we report that the electrophilic main-group cations thallium(III) and lead(IV) stoichiometrically oxidize methane, ethane, and propane, separately or as a one-pot mixture, to corresponding alcohol esters in trifluoroacetic acid solvent. Esters of methanol, ethanol, ethylene glycol, isopropanol, and propylene glycol are obtained with greater than 95% selectivity in concentrations up to 1.48 molar within 3 hours at 180°C. Experiment and theory support a mechanism involving electrophilic carbon-hydrogen bond activation to generate metal alkyl intermediates. We posit that the comparatively high reactivity of these d^{10} main-group cations relative to transition metals stems from facile alkane coordination at vacant sites, enabled by the overall lability of the ligand sphere and the absence of ligand field stabilization energies in systems with filled d-orbitals.

The world is undergoing a revolution in raw hydrocarbon feedstock supply with the discovery of increasingly abundant sources of natural gas in shale and offshore gas fields (*1*). Although natural gas is primarily methane, natural gas—particularly from shale—also has substantial amounts of ethane and propane (*2*). The conversion of methane, as well as these higher alkanes in natural gas, into liquid fuels and commodity chemicals such as methanol, ethylene, ethanol, ethylene glycol, isopropanol, and propylene glycol at lower costs than the current multistep, capital-intensive processes could reduce emissions and our dependence on petroleum, as well as increase the value of natural gas.

An important approach that has emerged in the past few decades is the design of molecular (homogeneous) catalysts for the oxidative functionalization of alkanes based on the CH activation reaction. This involves selective reaction of an M-X catalyst with a hydrocarbon CH bond (R-H) under relatively mild conditions without the involvement of radicals in order to generate a M-R intermediate that is converted to the desired R-X product with regeneration of M-X (Eq. 1). There has been considerable effort in this area of research with homogeneous (*3*–*23*) as well as heterogeneous catalysts (*24*–*26*), and substantial progress has been made in recent years. Most of the work on the homogeneous systems have been primarily based on transition metals (with unfilled d-shells, $d^{<10}$) such as Pt (*3*, *4*, *16*), Pd (*14*, *17*–*19*, *23*), Rh (*20*–*22*), and Ir (*7*–*10*). In contrast, relatively few studies have been directed toward the classic main-group elements with a filled d-shell (d^{10}). In 1993, we reported an example of a main-group metal cation, Hg^{II}, in the superacid concentrated H_2SO_4 for direct conversion of methane to methanol esters (*15*). In spite of the simplicity of the Hg^{II} system, it was not further developed because of lack of reaction in more practical, weaker acid media such as CF_3CO_2H (TFAH), CH_3CO_2H (HOAc), or aqueous acids with which product separation could be practical. Another key issue was that the reactions of ethane and propane were unselective with the Hg^{II} system. We originally proposed an electrophilic CH activation mechanism for the Hg^{II} system. However, later work by Sen, based on the observation of products resulting from C-C cleavage reactions with higher alkanes, suggested that Hg(II) in superacid media was sufficiently oxidizing to initiate free-radical reactions (*5*)

$$\text{M-X} + \text{R-H} \rightarrow \text{M-R} \rightarrow \text{M-X} + \text{R-X} \qquad (1)$$

This possibility for unselective radical reactions with higher alkanes was also considered by Moiseev and co-workers in the early 1990s on the reaction of alkanes in TFAH with strongly oxidizing salts that were known to be effective for oxidizing hydrocarbons through free-radical mechanisms (*27*, *28*). The initial report showed high yield and selectivity for the stoichiometric reactions of Co^{III} with methane to Me-TFA (*27*). Carrying out

[1]The Scripps Energy and Materials Center, Department of Chemistry, The Scripps Research Institute, Jupiter, FL 33458, USA. [2]Department of Chemistry and Biochemistry, Brigham Young University (BYU), Provo, UT 84602, USA.

*Corresponding author. E-mail: rperiana@scripps.edu (R.A.P.); dhe@chem.byu.edu (D.H.E.); bhashigu@scripps.edu (B.G.H.)